

Rapid Whole Slide Imaging via Learning-based Two-shot Virtual Autofocusing

Qiang Li, Xianming Liu, *Member, IEEE*, Kaige Han, Cheng Guo, Xiangyang Ji, *Member, IEEE*, and Xiaolin Wu, *Fellow, IEEE*

Abstract—Whole slide imaging (WSI) is an emerging technology for digital pathology. The process of autofocusing is the main influence of the performance of WSI. Traditional autofocusing methods either are time-consuming due to repetitive mechanical motions, or require additional hardware and thus are not compatible to current WSI systems. In this paper, we propose the concept of *virtual autofocusing*, which does not rely on mechanical adjustment to conduct refocusing but instead recovers in-focus images in an offline learning-based manner. With the initial focal position, we only perform two-shot imaging, in contrast traditional methods commonly need to conduct as many as 21 times image shooting in each tile scanning. Considering that the two captured out-of-focus images retain pieces of partial information about the underlying in-focus image, we propose a U-Net-inspired deep neural network based approach for fusing them into a recovered in-focus image. The proposed scheme is fast in tissue slides scanning, enabling a high-throughput generation of digital pathology images. Experimental results demonstrate that our scheme achieves satisfactory refocusing performance.

Index Terms—Virtual autofocusing, whole slide imaging, deep learning.

I. INTRODUCTION

WHOLE slide imaging (WSI), also referred to as *virtual microscopy* [1], [2], is applied to transform glass tissue slides to digital images. The interest in using WSI for digital pathology practice has steadily grown, since it provides a feasible approach to assist disease diagnosis by convenient visualization and navigation of tissue slide images in an interactive manner [3], [4]. A remarkable milestone is that in 2017 the US Food and Drug Administration has approved Philips' WSI system for the primary diagnostic use [5].

In a typical WSI system, different tiles of one tissue slide is scanned to obtain digital representations using a high-resolution objective lens, which are then aligned and stitched together to produce a complete and seamless image of the entire slide [6]. The numerical aperture (NA) of lens is usually high (typically larger than 0.75), and thus the resulting depth of field (DoF) is

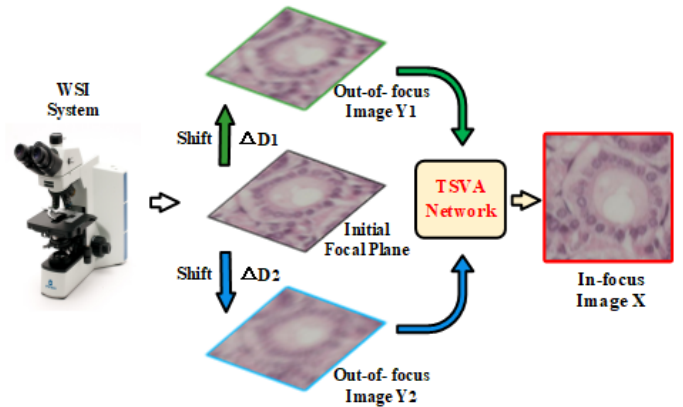


Fig. 1. Illustration of the proposed rapid whole slide imaging system via learning-based two-shot virtual autofocusing.

micron-sized. The small DoF in WSI systems poses a challenge to acquire in-focus images of tissue sections that are with uneven topography [7]. Thus the out-of-focus blurring artifact is the main cause of poor imaging quality in WSI [8]. To address this problem, the most popular approach in current WSI systems is the focus map surveying method [9], which creates a focus map prior to scanning. Specifically, for each point in the map, it scans the sample to different axial positions and acquires a z-stack that include many out-of-focus images, which are further processed according to some criterion, such as image contrast or entropy, to derive the ideal focal point for one tile position. This process is repeated for all tiles of the entire tissue slide. The mechanical system then brings the sample back to the right position to perform in-focus image shooting.

There are two major limitations for this well-established focus map surveying method. First, as stated above, for each tile it overall needs $N + 1$ times image shooting, where N is the number of out-of-focus images in a z-stack and is usually set as 20. The acquisition of a z-stack requires repetitive mechanical motions with cyclic acceleration and deceleration, which is time-consuming. Thus, creating a focus map for every tile requires a significant amount of overhead time. While selecting a subset of tiles for focus point surveying can save time to some extent, it comes at the expense of decreasing focusing accuracy and poor image quality. Second, since the derived ideal focal positions of different tiles are varying, focus map surveying puts forward higher requests to the mechanical system, which should have high positional accuracy and repeatability, in order to move the sample to the right position for the later scanning.

This work was supported by XX. (*Corresponding author: Xianming Liu*).

Q. Li, X. Liu, K. Han are with the School of Computer Science and Technology, Harbin Institute of Technology, Harbin 150001, China, and also with the Peng Cheng Laboratory, Shenzhen 518052, China (qiangli0120@hit.edu.cn; csxm@hit.edu.cn; 18S103171@stu.hit.edu.cn).

C. Guo is with the School of Measurement Science, Harbin Institute of Technology, Harbin 150001, China (guocheng_27@163.com).

X. Ji is with the Department of Automation, Tsinghua University, Beijing 100084, China (xyji@tsinghua.edu.cn).

X. Wu is with the Department of Electrical and Computer Engineering, McMaster University, Hamilton, ON L8S 4L8, Canada, and also with the School of Electronic Information and Electrical Engineering, Shanghai Jiao Tong University, Shanghai 200240, China (xwu@ece.mcmaster.ca).

Some hardware-assisted methods are presented to tackle the challenges listed above. For example, the setups of dual camera [10] and two LEDs [11] are proposed to reduce the number of axial scanning. However, the use of the additional hardware is not compatible with most existing WSI platforms.

In this paper, we propose a novel whole slide imaging system with reduced scanning time cost and complete system compatibility. Different from traditional autofocusing methods that rely on mechanical adjustment to conduct refocusing, we propose the concept of *virtual autofocusing*, which instead recover in-focus images in a learning-based manner, as illustrated in Fig. 1. Specifically, at the very beginning, for the first tile, we collect a z-stack with dense images, according to which we obtain the initial focal position. Then for the rest tiles, we perform two-shot imaging, where the z-stack contain only two out-of-focus images, which are captured in both sides of the initial focus with relative defocus offsets. This setup reduces the requirement of positional accuracy of the mechanical system, enabling a low-cost option. With these dual captured images, we no longer create the focus map and perform autofocusing during the process of tissue slide scanning, but recover the in-focus one offline with the help of large amounts of training data and high-performance computing devices such as GPU. In particular, considering the two-shot out-of-focus images retain pieces of partial information about the underlying in-focus image, we propose a U-Net-inspired deep neural network based approach for fusing them into a recovered in-focus image. Experimental results demonstrate that our scheme achieves satisfactory refocusing performance.

In summary, our scheme enjoys the following merits:

- **High-speed and High-throughput:** Compared with traditional methods that conduct as many as 21 times image shooting in each tile scanning to create z-stack for focus map, our scheme only performs twice shooting instead of focus map surveying, which significantly reduces the overhead time cost. Moreover, our method does not perform autofocusing in the process of slide scanning, but recovers the underlying sharp image using an offline learning strategy. Therefore, it owns high scanning speed, which enables a high-throughput generation of digital pathology images.
- **High Imaging Quality:** The one-shot method has to exploit the additional constraints for the one out-of-focus image [12]. More specifically, the single out-of-focus image contains complex features, resulting from the non-negligible sample thickness and inevitable optical aberrations. However, the proposed two-shot method utilizes more partial information about the underlying in-focus image from two out-of-focus images to fuse the features of mutual compensation. Therefore, the two-shot method has the higher imaging quality than the single one.
- **System Compatibility:** Our method does not involve any hardware modifications to current WSI systems. In contrast, other deep learning based autofocusing methods, such as Pinkard *et al.* [13] and Jiang *et al.* [14], need the addition of one or more LEDs to achieve refocusing based on two-shot images.

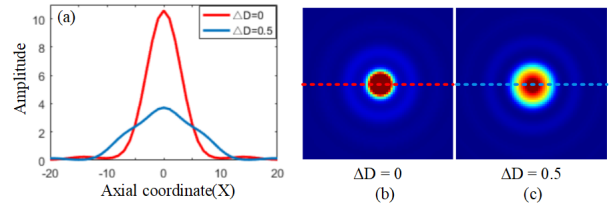


Fig. 2. (a) The axial PSF distribution curve with in-focus position (red line) and defocus position (blue line). (b) The lateral plane with $\Delta D = 0$. (c) The lateral plane with $\Delta D = 0.5 \mu\text{m}$.

The paper is organized as follows: Section II overviews some related works. Section III introduces the problem formulation and the motivation of the proposed scheme, Section IV details the proposed in-focus image recovery method, and Section V provides the experimental results. We conclude this paper in Section VI.

II. RELATED WORK

In this section, we provide a brief review about existing autofocusing methods, which can be generally divided into two categories: software-based and hardware-based. These two kinds of methods are sometimes combined to achieve satisfactory performance.

The basic idea of software-based autofocusing is to capture one or more out-of-focus images and use them to determine the ideal focal position. The most popular approach of this kind is focus map surveying [9]. It captures a z-stack along the optical axis including a series of out-of-focus images with different relative distance offset [15], and then maximizes image contrast to determine the ideal focal plane. Software-based methods are usually slow due to the requirement of a full focal stack. Moreover, image contrast does not always serve as a good image quality metric. For example, some pathology samples that are weakly stained have low image contrast.

Hardware-based methods attempt to directly measure the distance from the objective lens to the sample, and thus is rapid. Among hardware-based approaches, Liron *et al.* [16] proposed to use an external light source or laser to measure the position of a reference point. Montalto *et al.* [10] proposed to utilize a secondary camera to decouple image acquisition from focusing and allow parallel processing. Liao *et al.* [9] developed a novel focus map surveying method using additional LED illumination and autocorrelation image analysis. This kind of methods need to introduce hardware modifications to the microscope, which can be expensive and not compatible to current WSI systems.

With the emergence of deep learning in microscopy, convolutional neural networks (CNNs) based approaches have appeared for autofocusing. The work in [14] is the first one in the literature that uses CNN to predict the focal position. Specifically, Jiang *et al.* [14] firstly acquired $\sim 130,000$ images with different defocus distances as the training dataset, and used an end-to-end deep residual network to build the relationship between the input image and its focal distance. This approach is able to capture images on the fly without focus map surveying. However, despite this method achieves remarkable autofocusing performance, from the perspective of methodology, it is not easy

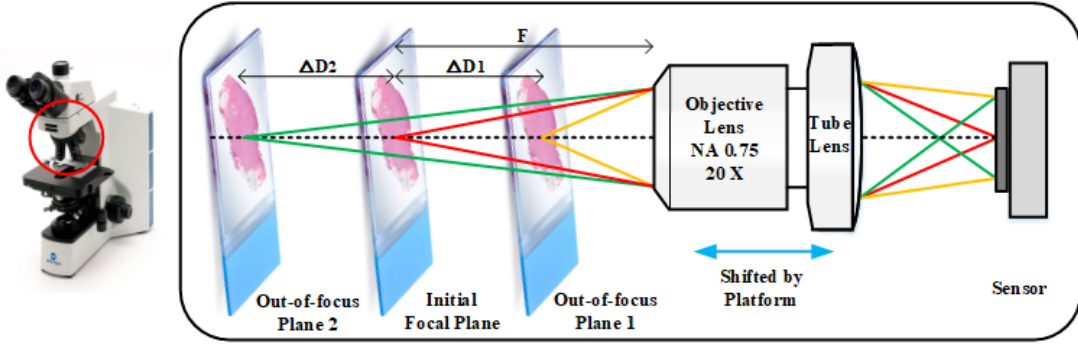


Fig. 3. Illustration of the microscopy imaging model of the proposed WSI system.

to derive a model that accurately describes the relationship between an image with complex contents and a numerical value (the defocus distance). More recently, Pinkard *et al.* [13] proposed to combine the hardware modification and deep learning. It requires the addition of one or a few off-axis LEDs to a conventional transmitted light microscope. Defocus distance is then estimated and corrected based on a single image under this LED illumination using a neural network.

III. PROBLEM FORMULATION

Traditional autofocusing methods rely on mechanical adjustment to conduct refocusing, which need repetitive axial scanning. In order to reduce the time cost of scanning, we propose the concept of *virtual autofocusing*, which no longer performs time-consuming mechanical autofocusing but instead recovers in-focus images in a learning-based manner. In this section, we introduce the problem formulation and the motivation of the proposed scheme.

A. Optical Model

In optical microscopy, the point spread function (PSF) can be formulated by the Born & Wolf model [17], [18]:

$$h(r, \Delta D) = \left| C \int_0^1 J_0 \left(k \frac{\text{NA}}{n} r \rho \right) e^{-\frac{1}{2} i k \rho^2 \Delta D \left(\frac{\text{NA}}{n} \right)^2} \rho d\rho \right|^2, \quad (1)$$

where r is the radial distance along the lateral plane; ΔD is the distance between the in-focus position and the imaging plane along the optical axis, *i.e.*, the defocus distance; C is a normalization constant; J_0 is zero-order Bessel function of the first kind; k is angular wave number of the light source; n is the refractive index; i is the imaginary number; ρ is the normalized coordinate in the exit pupil. The axial PSF model is shown in Fig. 2 (a) and the lateral planes with different ΔD are shown in Fig. 2 (b) and (c). It can be found that, the amplitude of blue line ($\Delta D = 0.5 \mu\text{m}$) is lower than the red one ($\Delta D = 0$) due to the out-of-focus aberration, which becomes larger as ΔD increases.

Accordingly, to recover the in-focus image, it is reasonable to assume that the most reliable knowledge is from the two nearest out-of-focus planes of the in-focus plane [19], [20]. In contrast, the single out-of-focus image has complex features which need to be restrained, due to the effects of sample thickness and

optical aberrations. Therefore, the two-shot method with feature fusion and compensation has the better performance than the single one.

B. Infocusing and Defocusing Model

In WSI, samples of pathological tissue slices are with uneven depth variations, and thus the ensuing PSFs vary spatially. Based on the layered depth of field model [21], the continuous depth map is translated to discrete depth layers (image planes), and the PSF $h(r, \Delta D)$ is replaced by h_m , where m stands for the position of each depth layer and h_0 is the PSF of the in-focus depth. Each depth layer is blurred by its corresponding PSF with a convolution operation and the blurred depth layers are integrated to form the captured image. Therefore, the in-focus imaging model can be expressed as:

$$X = \sum_m x_m \otimes h_m, \quad (2)$$

where x_m is the discrete depth layer of sample with depth m and x_0 is the in-focus object plane of sample, \otimes is the convolution operator, X is the underlying in-focus image of x_0 . When the sample is shifted by offset ΔD_1 from the in-focus object plane, we denote the new in-focus object plane as x_i . Similarly, the new in-focus object plane is denoted as x_j when the sample is shifted by offset ΔD_2 . Accordingly, the captured out-of-focus images Y_1 and Y_2 can be represented as:

$$Y_1 = \sum_m x_{m+i} \otimes h_m, \quad Y_2 = \sum_m x_{m+j} \otimes h_m. \quad (3)$$

The defocusing imaging model indicates that recovering in-focus image from out-of-focus images in WSI is more challenging than the conventional inverse imaging problem. Fortunately, the two-shot out-of-focus images retain pieces of partial information about the underlying in-focus image, which inspires us to fuse them to derive the sharp image by a deep neural network.

C. Virtual Autofocusing

In view of the above, we propose a learning-based virtual autofocusing strategy relying on two-shot images, which are from the two nearest out-of-focus planes on both sides of the initial focal plane, as illustrated in Fig. 3. Specifically, at

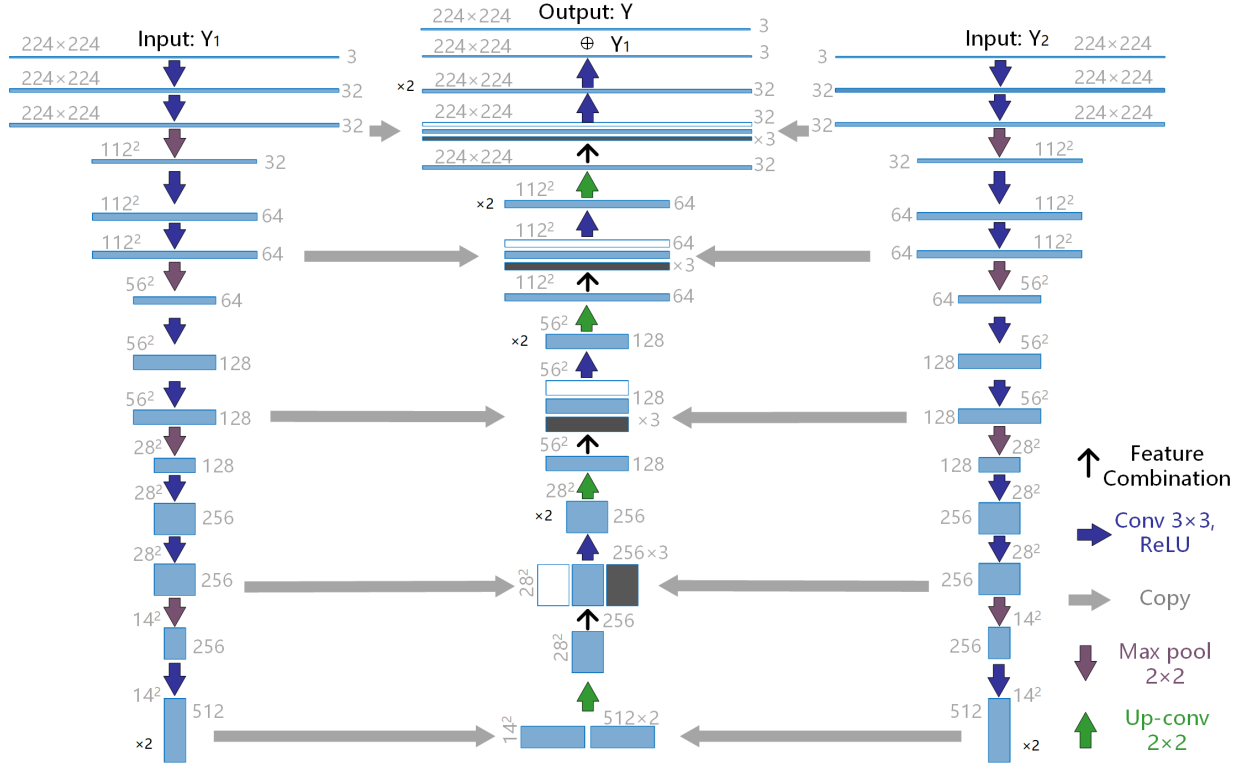


Fig. 4. The architecture of the proposed TSVA network. Each blue box corresponds to a multi-channel feature map. The number of channels is denoted at the side edge of the box. The x-y-size is provided at the top edge of the box. White boxes represent copied feature maps of the left contracting path. Black boxes represent copied feature maps of the right contracting path. The colorful arrows denote the different operations. $\times 2$ stands for an additional convolution.

the very beginning, for the first tile we collect a full z-stack to derive the initial focal position F . It is worth noting that, since different tiles are with uneven topography, this position is usually not the focal one of other tiles. Then for the rest tiles, two out-of-focus images are captured with relative defocus offset ΔD_1 and ΔD_2 to F respectively. This setting is inspired by the operation of manual microscopy, which first performs coarse tuning to get a best possible picture and further conducts fine tuning to finally acquire the best one.

In conclusion, the practical workflow of the proposed method is listed as:

- **Initial focal plane prediction:** For the first tile, we collect a z-stack and obtain the initial focal position.
- **Two-shot imaging:** For the rest tiles, we perform two-shot imaging, which are captured in both sides of the initial focal plane with relative defocus offsets.
- **Algorithm processing:** The in-focus image can be recovered directly offline by algorithm processing.

The following task is to recover X by fusing its two observations Y_1 and Y_2 . This is done in our scheme through a U-Net-inspired deep neural network, which will be elaborated in the next section. In practical implementation, we set $\Delta D_1 = \Delta D_2 = \Delta D$.

IV. THE PROPOSED IN-FOCUS IMAGE RECOVERY METHOD

With the dual captured images, we then try to recover the in-focus image with the help of large amounts of training data

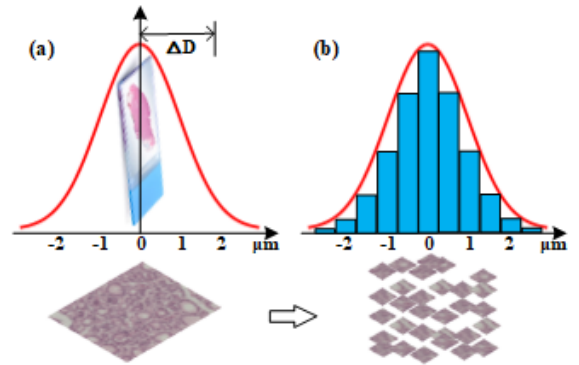


Fig. 5. Illustration of Gaussian distribution of focal positions. (a) The Gaussian distribution of focal positions with ΔD . The bottom tile shows the continuous fluctuations in the surface of the sample. (b) The discrete Gaussian distribution of focal positions with ΔD . The bottom patches segmented from tiles exhibit the discrete offset of the sample.

and high-performance computing environment. The proposed method is built upon an elegant deep neural network, the so-called U-net [22]. We modify and extend this architecture such that it can work with two input images and yield a recovered sharp image. In the following, we will introduce the network architecture and the training process in detail.

A. Network Architecture

The proposed deep neural network that is tailored for two-shot virtual autofocusing (TSVA) is illustrated in Fig. 4.

TABLE I
OBJECTIVE PERFORMANCE COMPARISON WITH RESPECT TO PSNR (DB) OF FOUR COMPARED METHODS.

Methods	ΔD	Sample 1	Sample 2	Sample 3	Sample 4	Sample 5	Sample 6	Average
Dark Channel [23]	$0.5\mu\text{m}$	31.67 ± 1.69	29.92 ± 0.80	33.89 ± 0.88	33.56 ± 4.66	32.19 ± 3.10	30.30 ± 4.69	32.42 ± 3.85
Graph Deblur [24]		30.57 ± 15.59	51.76 ± 0.50	17.27 ± 3.87	22.85 ± 8.24	21.09 ± 3.85	22.97 ± 3.37	26.67 ± 12.79
Burst U-net [25]		39.48 ± 1.26	38.83 ± 0.84	40.62 ± 0.26	39.44 ± 0.56	39.81 ± 0.94	40.41 ± 1.22	39.60 ± 0.95
TSVA		44.83 ± 1.48	48.04 ± 0.40	48.35 ± 0.30	49.29 ± 1.00	49.61 ± 0.31	50.06 ± 0.54	48.71 ± 1.64
Dark Channel [23]	$1\mu\text{m}$	30.74 ± 0.90	28.50 ± 0.05	32.76 ± 0.30	33.37 ± 1.16	30.95 ± 4.46	30.35 ± 2.77	31.74 ± 2.77
Graph Deblur [24]		28.91 ± 9.04	38.79 ± 0.33	17.98 ± 1.50	19.03 ± 3.42	17.38 ± 5.09	20.34 ± 4.09	21.78 ± 7.74
Burst U-net [25]		36.37 ± 0.17	35.56 ± 0.03	38.03 ± 0.04	37.28 ± 0.26	37.70 ± 0.54	38.50 ± 0.81	37.31 ± 0.89
TSVA		37.13 ± 0.34	39.16 ± 0.34	39.81 ± 0.24	40.37 ± 0.36	40.44 ± 0.16	41.35 ± 0.78	39.93 ± 1.34
Dark Channel [23]	$1.5\mu\text{m}$	30.35 ± 0.89	28.15 ± 1.28	33.65 ± 0	32.99 ± 0.67	32.43 ± 0	31.88 ± 0.84	31.35 ± 1.73
Graph Deblur [24]		20.77 ± 8.46	37.50 ± 0.65	10.62 ± 0	20.55 ± 1.33	19.17 ± 0	23.82 ± 4.49	22.19 ± 7.78
Burst U-net [25]		34.27 ± 0.58	36.84 ± 0.20	37.32 ± 0	36.80 ± 0.47	37.49 ± 0	36.92 ± 0.58	35.88 ± 1.40
TSVA		35.18 ± 0.48	38.05 ± 0.56	38.91 ± 0	39.09 ± 0.29	39.19 ± 0	39.77 ± 0.44	37.58 ± 2.02
Dark Channel [23]	$2\mu\text{m}$	28.15 ± 0.52	28.06 ± 0.54	31.06 ± 0	32.31 ± 0.71	32.28 ± 0	30.92 ± 0	29.94 ± 1.95
Graph Deblur [24]		31.61 ± 0.67	36.03 ± 0.26	19.98 ± 0	18.77 ± 0.12	26.79 ± 0	24.10 ± 0	27.53 ± 6.47
Burst U-net [25]		32.57 ± 0.20	35.23 ± 1.05	36.11 ± 0	36.10 ± 0.27	36.34 ± 0	36.86 ± 0	34.97 ± 1.71
TSVA		33.01 ± 0.20	36.54 ± 0.21	37.23 ± 0	37.85 ± 0.24	38.59 ± 0	39.84 ± 0	36.35 ± 2.38
Dark Channel [23]	$2.5\mu\text{m}$	28.32 ± 0.64	-	-	-	31.53 ± 0	-	29.39 ± 1.60
Graph Deblur [24]		17.29 ± 1.06	-	-	-	20.25 ± 0	-	18.27 ± 1.64
Burst U-net [25]		30.80 ± 0.28	-	-	-	35.84 ± 0	-	32.48 ± 2.39
TSVA		31.30 ± 0.33	-	-	-	38.13 ± 0	-	33.58 ± 3.23
Dark Channel [23]	$3\mu\text{m}$	-	-	-	-	30.94 ± 0	-	30.94 ± 0
Graph Deblur [24]		-	-	-	-	12.66 ± 0	-	12.66 ± 0
Burst U-net [25]		-	-	-	-	34.86 ± 0.20	-	34.86 ± 0
TSVA		-	-	-	-	36.12 ± 0	-	36.12 ± 0

Specifically, the TSVA network consists of two contracting paths (left and right sides) that are with two out-of-focus images Y_1 and Y_2 as inputs, and an expansive path (middle side) that outputs the recovered in-focus image X . The sharper image of two captured ones is chosen as Y_1 , according to the metric of Brenner gradient [26].

- **Contracting paths design:** The contracting paths employ the typical convolutional architecture, including the repeated use of two 3×3 convolutions followed by a rectified linear unit (ReLU) and 2×2 max pooling downsampling layer with stride 2. We double the number of feature channels at every downsampling step. These two paths share the same parameters. Finally, we combine the deepest layers of two paths into a cascaded one.
- **Expansive path design:** The expansive path in each step includes an upsampling feature layer followed by 2×2 convolution (up-convolution), which halves the number of feature channels. We build a concatenation with the corresponding feature maps from the left contracting path (white layer) and the right contracting path (black layer), and employ two 3×3 convolution followed by ReLU. At the final residual layer, Y_1 is added to generate the recovered in-focus image X . In total the network has 27 convolutional layers.

B. Network Training

1) *Training Dataset:* We use a part of the dataset collected by Jiang *et al.* [14] to train our network. The dataset includes 35 research-grade human pathology slides with Hematoxylin and eosin stains (Omano OMSK-HP50), and contains 162 pathological tissue z-stack tiles. For each tile there is a stack of 41 images taken with different focal distances in a step size of $0.5\mu\text{m}$, ranging from $-10\mu\text{m}$ to $10\mu\text{m}$, with $0\mu\text{m}$ corresponding to the image in focus. The in-focus image

is recovered by maximizing Brenner gradient of the z-stack images.

In image stacks of all tiles, the focal distance of an out-of-focus image is given as the defocus offset to the image in focus. But in our system, the microscope camera makes two shots of each tile at two prefixed focal distances. Therefore, we need the out-of-focus images of absolute focal distances to train our TSVA network. We convert the training images in relative focal distance in the dataset of [14] to those in absolute focal distance by simply adding a Gaussian random variable $n \sim \mathcal{N}(0, 1)$ to the relative focal distance. This is because, according to the observation of [27], the focal positions follow a Gaussian distribution, as shown in Fig. 5 (a). Specifically, The images of slides are divided into 224×224 patches in Fig. 5 (b). Then, we convert the dataset to discrete patches of Gaussian distribution. There are 3240 patches in the initial dataset and we enlarge the dataset by rotation.

2) *Implementation Details:* Here we clarify some details in implementation. In network training, the loss function is defined as follows:

$$L = \frac{1}{N} \sum_{i=1}^N (X_i - \tilde{X}_i)^2, \quad (4)$$

where X_i is the ground-truth in-focus image and \tilde{X}_i is the network output, and N is the number of training images in each batch. We select 85% patches with labeled relative defocus offset ΔD as our training set and 15% patches for verification. We utilize batch normalization with batch size as 20 for acceleration training. The network is trained using the ADAM optimizer with a learning rate as 0.0005 for 50 epochs. The network training is run on a single NVIDIA GTX 1080Ti.

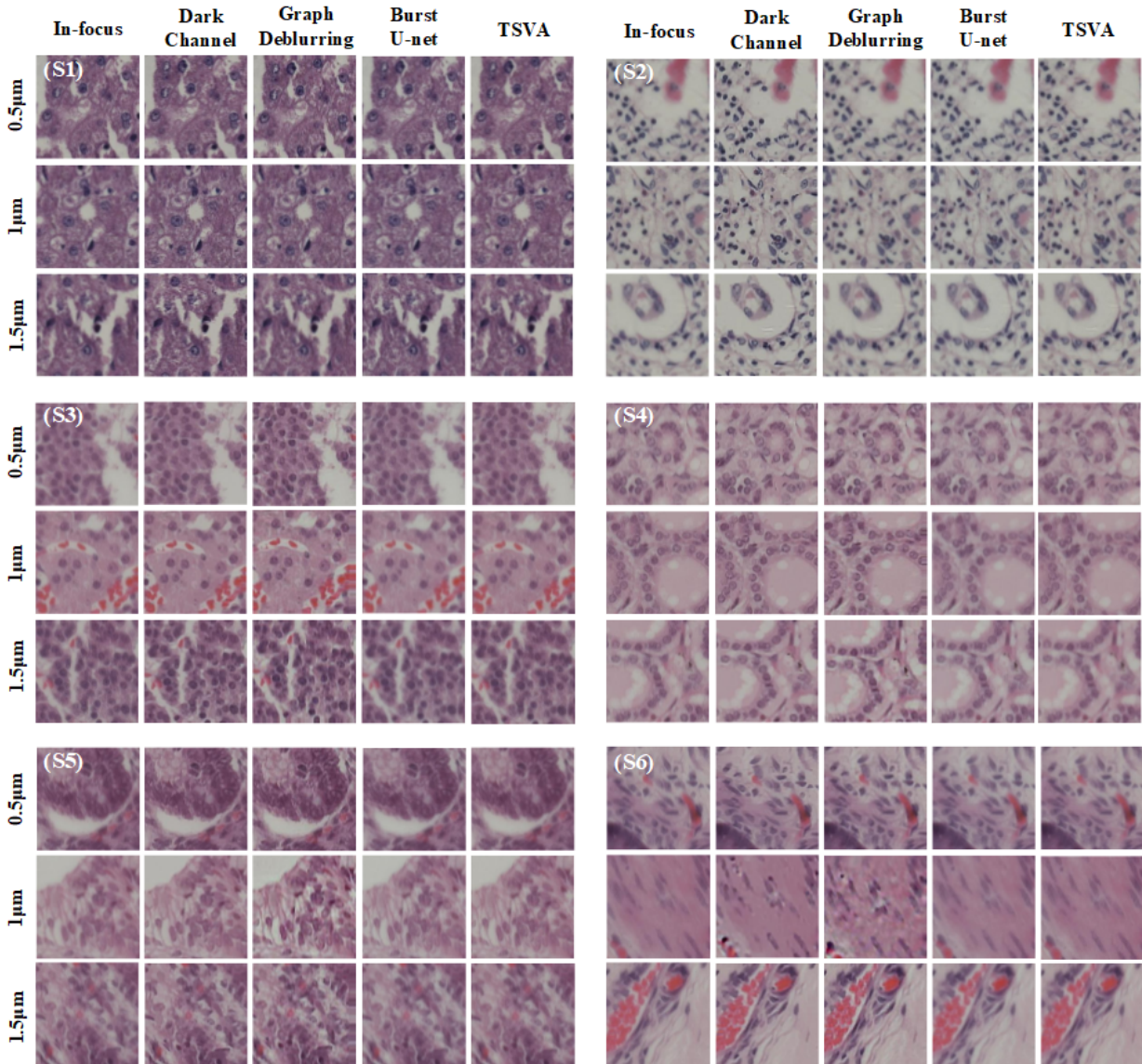


Fig. 6. Subjective performance comparison on *Sample1* to *Sample6*. Please enlarge the PDF for more details.

V. EXPERIMENTS

In this section, we provide extensive experimental results to demonstrate the effectiveness of our proposed TSVA scheme.

The experimental analysis is conducted on two test datasets:

- **Dataset 1:** We use the part of Dataset 1 [14] except that for training as the test set. It contains all stained tissue slide images, including six categories of biological tissues with different morphological characteristics of size, thickness and structure, named *Sample1* to *Sample6*.
- **Dataset 2:** Dataset 2 [14] that contains the de-identified HE skin-tissue slides made by the Dermatology Department of the UConn Health Center is also used for testing, which is collected from different source with the training set. It includes seven categories of biological tissues named *Sample7* to *Sample13*.

For both datasets, the size of each tile image is 1224×1024 . We select test images with the corresponding relative defocus

offset ΔD ranging from $-3\mu m$ to $+3\mu m$ with interval $0.5\mu m$, which are also converted in the same way as the training data. There are 340 and 640 patches in Dataset 1 and Dataset 2 respectively.

A. Comparison with State-of-the-arts

In this subsection, to demonstrate the effectiveness of the proposed in-focus image recovery scheme, we provide objective and subjective quality comparison on Dataset 1 with state-of-the-art image deblurring methods, including dark channel prior based [23], graph-prior based [24], U-net based burst deblurring [25] that also takes multiple images as inputs.

The objective performance evaluation with respect to PSNR is shown in Table I, where “-” represents there is no corresponding image in this defocus distance. It can be found that, our method achieves the best PSNR performance on all sample

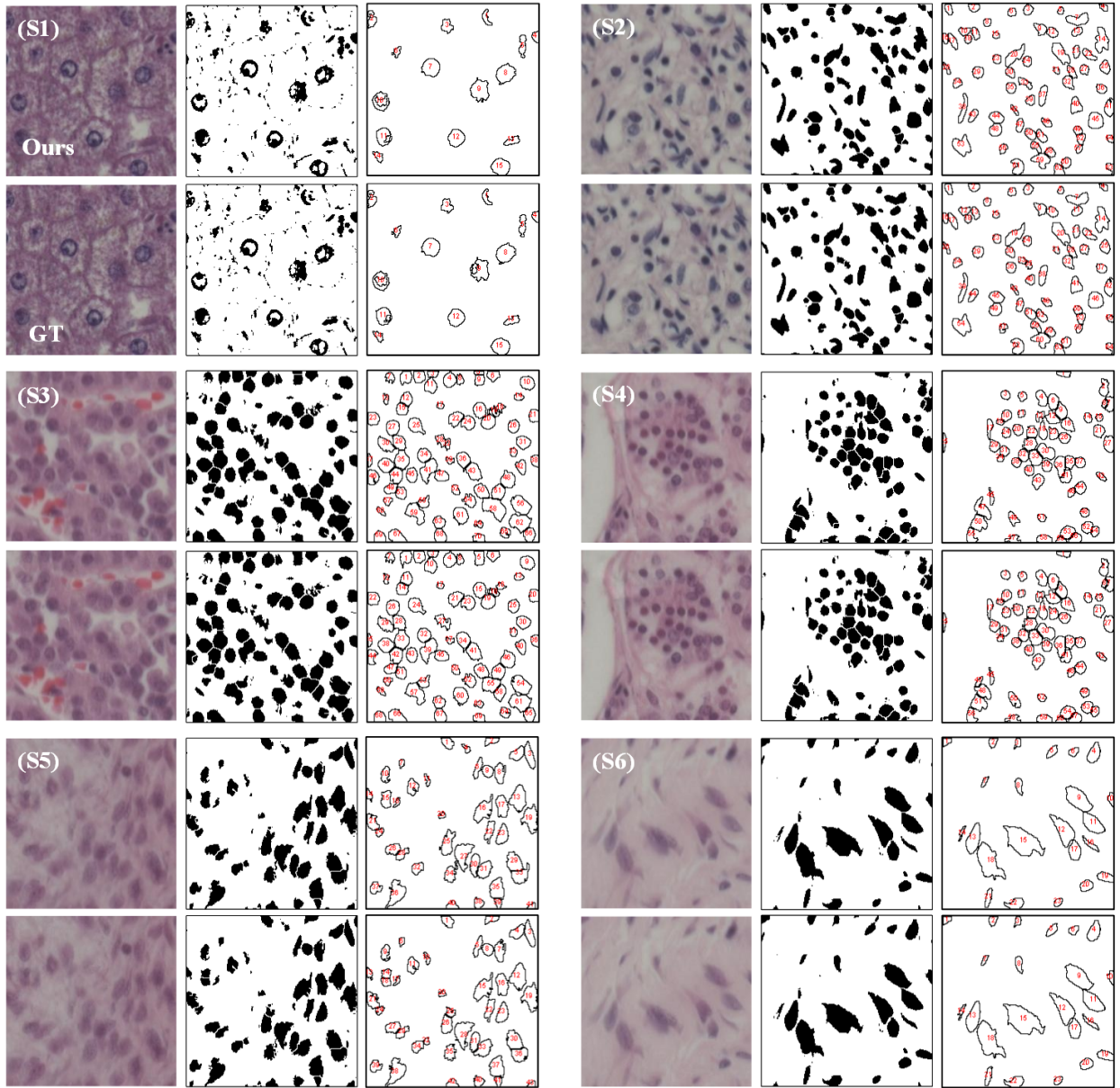


Fig. 7. Influence of image quality to the accuracy of cell counting. For (S1) to (S6), the cell counting results on our generated image are at the top and the corresponding results of ground-truth are at the bottom. From left to right, the input image for cell counting, the cell segmentation image, and the image of cell outlines counting. Please enlarge the PDF for more details.

images. These comparison results demonstrate the superior performance of our proposed TSVA network.

The subjective comparison results on six test images are illustrated in Fig. 6. The ground-truth in-focus images are also offered as the quality reference. From the results, it can be found that the statistical prior-based methods, *i.e.*, [23] and [24], cannot handle complicated out-of-focus effects in WSI, since the statistics of biomedical images is different from natural images. These two methods cannot preserve texture information well. Burst U-net based method [25], which also uses deep neural network for burst deblurring, achieves better subjective performance than [23] and [24]. Our method achieves the best subjective performance among compared methods. The recovered in-focus images share a very close subjective effect

with the ground-truth in-focus images.

B. Influence of Image Quality to Downstream Image Analysis

According to Fig. 6, it is hard to differentiate the recovered in-focus images from the ground-truth by human eyes. Another concern is whether the machine also cannot differentiate them, *i.e.*, whether the recovered in-focus images would significantly reduce the accuracy of downstream image analysis tasks?

In this subsection, using cell counting that is a typical task of pathology image analysis as an example, we examine the influence of the quality of images yielded by the proposed visual autofocusing approach to the counting accuracy. We utilize a widely used tool *ImageJ*¹ [28] released by National

¹<https://imagej.nih.gov/ij/>

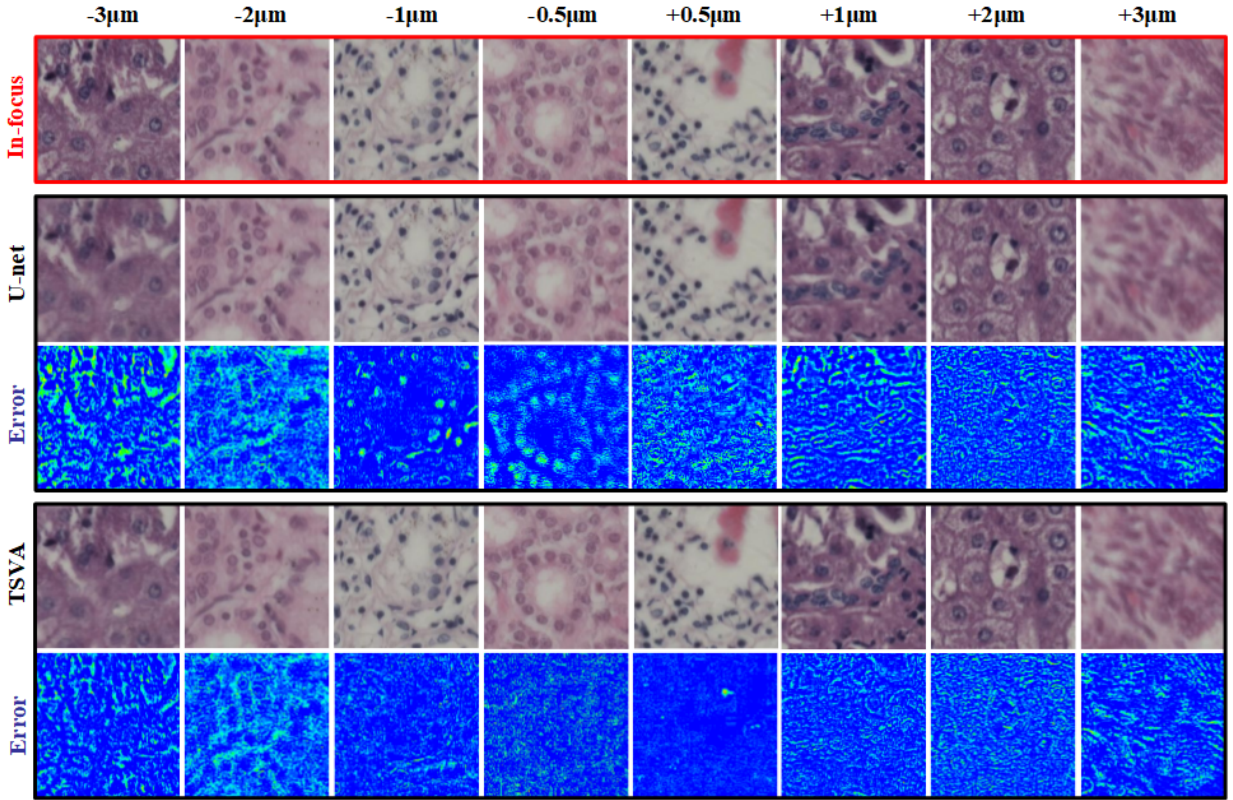


Fig. 8. Subjective Performance Comparison on images of Dataset 1. Please enlarge the PDF for more details. The in-focus images in red block are ground truth. The results of U-net and TSVA are shown in the two black blocks with the corresponding error maps on the bottom.

TABLE II
THE AVERAGE NUMBERS OF COUNTED CELLS WITH RESPECT TO DIFFERENT ΔD ON ALL SAMPLES IN DATASET 1.

ΔD	Sample 1		Sample 2		Sample 3		Sample 4		Sample 5		Sample 6		Average	
	Ours	GT	Ours	GT	Ours	GT	Ours	GT	Ours	GT	Ours	GT	Ours	GT
0.5 μm	15.17	15.5	42.38	42.13	22.4	22.4	19.4	19.36	18.75	19	22.75	23	22.38	22.43
1 μm	12.83	13.16	39.67	40	18.5	19.5	21.12	21.18	18.43	18.86	18.17	17.83	20.25	20.42
1.5 μm	14.44	14.56	32	33	33	33	25.5	25.67	21	21	25	25.5	21.78	22.05
2 μm	15.33	16	34.5	34	29	28	21	22	23	22	18	17	22.70	22.7
2.5 μm	10	10	-	-	-	-	-	-	28	27	-	-	16	15.67
3 μm	-	-	-	-	-	-	-	-	27	29	-	-	27	29
Average	14.00	14.27	39.40	39.40	23.44	23.56	20.78	20.84	19.70	19.96	21.20	21.20	21.57	21.69

Institutes of Health (NIH) as the test platform, which conducts cell counting including the following four steps: 1) gray processing; 2) adjusting brightness and contrast; 3) thresholding; 4) analysis of cell counting.

The in-focus images recovered by our method and the ground-truth in-focus images are taken as input to *ImageJ*, respectively. The results of cell counting are illustrated in Fig. 7. It can be found that, the cell counting results on our recovered images are very close to the results on the corresponding ground-truth images. In Table II, we also show the comparison of numbers of counted cells with respect to different ΔD on *Sample1* to *Sample6*. It can be seen that, compared with the results on the ground-truth (GT), the average cell counting error on our recovered in-focus images is 0.12, which is too small to reduce the accuracy of downstream analysis significantly.

C. Ablation Study

In this subsection, we provide the empirical ablation analysis of the proposed TSVA network. According to the TSVA architecture, there are two input out-of-focus images with relative defocus offsets ΔD . Therefore, it is essential to analyze the influence of dual input images and relative defocus offsets to the final performance. Moreover, we provide the study of the robustness of the proposed scheme to different test sets. Considering that our TSVA is built upon the U-net, we employ the traditional U-net [22] as the baseline, which takes Y_1 as input with different relative distance offsets.

1) *Influence of dual input images*: In this part, we provide empirical analysis if the dual captured images is really helpful to improve the quality of recovered in-focus images compared with the single one.

Table III shows objective performance comparison of U-net

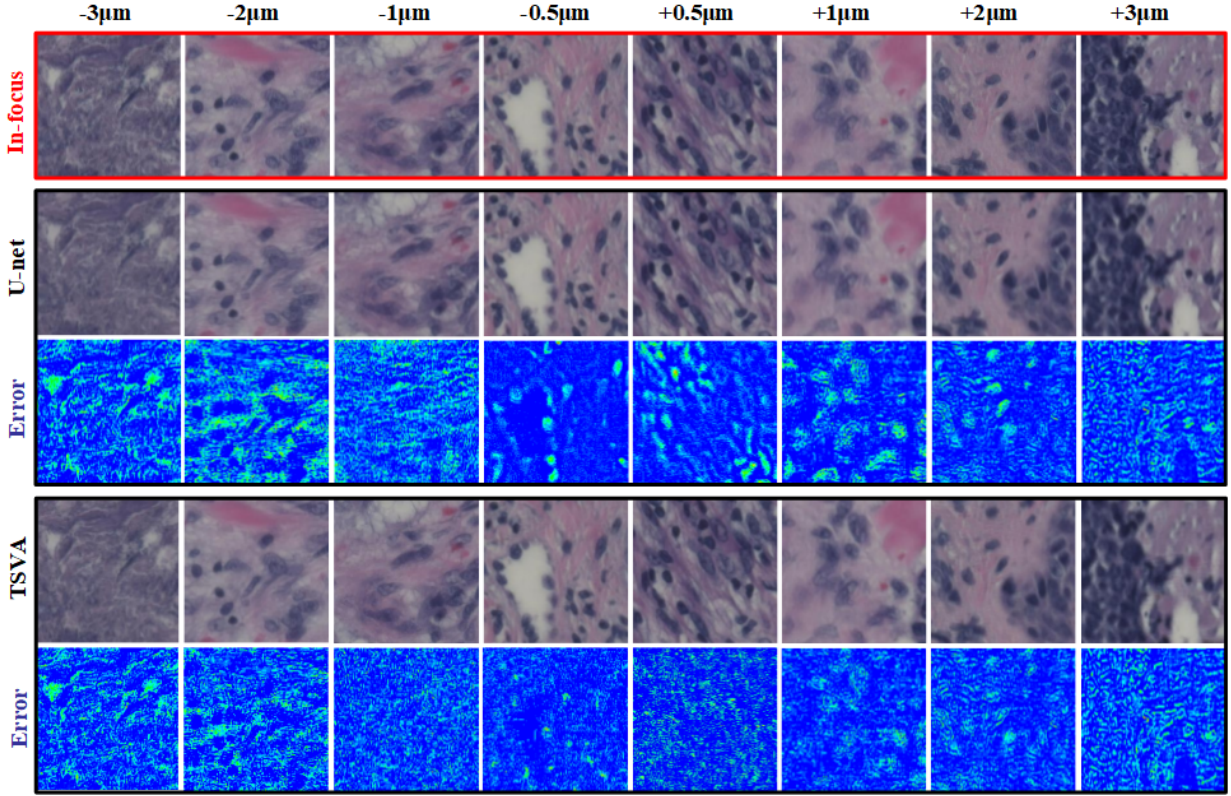


Fig. 9. Subjective Performance Comparison on images of Dataset 2. Please enlarge the PDF for more details. The in-focus images in red block are ground truth. The results of U-net and TSVA are shown in the two black blocks with the corresponding error maps on the bottom.

TABLE III
PSNR PERFORMANCE COMPARISON OF U-NET AND TSVA ON DATASET 1 AND DATASET 2 WITH RESPECT TO DIFFERENT ΔD .

Dataset	Methods	Relative Distance Offset ΔD (The mean on the top and standard deviation (SD) on the bottom in each methods)							Average
Dataset 1	U-net	ΔD	-3 μm	-2.5 μm	-2 μm	-1.5 μm	-1 μm	-0.5 μm	39.44 \pm 3.76
		PSNR	27.96 \pm 0	33.46 \pm 4.17	38.28 \pm 1.28	37.42 \pm 2.86	38.86 \pm 1.97	41.61 \pm 4.08	
		0 μm	+0.5 μm	+1 μm	+1.5 μm	+2 μm	+2.5 μm	+3 μm	
	TSVA	ΔD	-3 μm	-2.5 μm	-2 μm	-1.5 μm	-1 μm	-0.5 μm	42.25 \pm 4.90
		PSNR	30.11 \pm 0	33.58 \pm 2.74	38.60 \pm 1.07	38.34 \pm 1.87	39.82 \pm 1.11	47.99 \pm 1.59	
		0 μm	+0.5 μm	+1 μm	+1.5 μm	+2 μm	+2.5 μm	+3 μm	
		39.61 \pm 1.32	48.71 \pm 1.64	39.93 \pm 1.34	37.58 \pm 2.02	36.35 \pm 2.38	33.58 \pm 3.23	36.12 \pm 0	
Dataset 2	U-net	ΔD	-3 μm	-2.5 μm	-2 μm	-1.5 μm	-1 μm	-0.5 μm	38.83 \pm 2.95
		PSNR	33.22 \pm 0.34	34.82 \pm 1.74	36.27 \pm 1.65	37.76 \pm 1.29	38.61 \pm 0.99	41.28 \pm 3.23	
		0 μm	+0.5 μm	+1 μm	+1.5 μm	+2 μm	+2.5 μm	+3 μm	
	TSVA	ΔD	-3 μm	-2.5 μm	-2 μm	-1.5 μm	-1 μm	-0.5 μm	42.32 \pm 4.67
		PSNR	34.87 \pm 0.45	35.61 \pm 1.20	37.20 \pm 1.04	38.65 \pm 0.63	39.78 \pm 0.62	48.39 \pm 0.91	
		0 μm	+0.5 μm	+1 μm	+1.5 μm	+2 μm	+2.5 μm	+3 μm	
		39.55 \pm 0.57	48.55 \pm 0.88	39.77 \pm 0.60	38.26 \pm 0.79	36.61 \pm 1.32	35.23 \pm 0.79	33.89 \pm 0.00	

that takes Y_1 as input and our TSVA that takes Y_1 and Y_2 as inputs. It can be found that, on Dataset 1 and 2, TSVA achieves better PSNR performance than U-net for all cases. The average PSNR gains are 2.81dB and 3.49dB over U-net, respectively.

We also provide subjective performance comparison of U-net and TSVA in Fig. 8 on Dataset 1. For clear display, we show the error maps between the recovered in-focus images and the corresponding ground-truth. It can be seen that, compared with U-net, the structure errors produced by TSVA are smaller, in particular when ΔD is ranging from from $-1\mu m$ to $+1\mu m$.

Therefore, the proposed TSVA network achieves superior performance than U-net, benefiting from the dual inputs.

2) *Influence of different relative defocus offsets*: In this part, we examine the influence of different relative defocus offsets to the final performance.

The PSNR histograms with respect to ΔD on Dataset 1 and Dataset 2 are shown in Fig. 10 and Fig. 11 respectively. It can be found that: i) For different ΔD , the proposed TSVA always achieves higher PSNR values than U-net. This demonstrate that the performance of our scheme is robust with respect to ΔD . ii) The highest PSNR gains appear when $\Delta D = +0.5 \mu m$ and

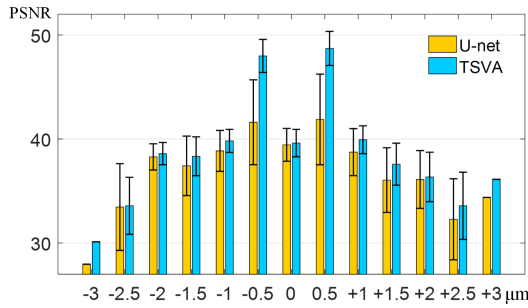


Fig. 10. PSNR performance comparison of U-net and TSVA on Dataset 1 with respect to different ΔD .

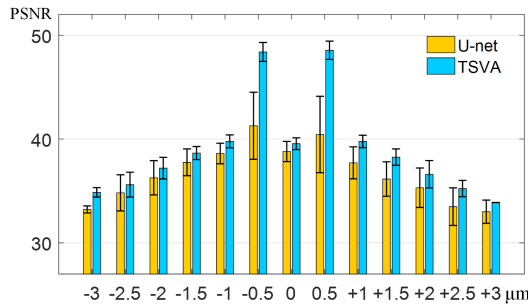


Fig. 11. PSNR performance comparison of U-net and TSVA on Dataset 2 with respect to different ΔD .

$\Delta D = -0.5 \mu\text{m}$. In practical case, most of estimated focal positions also lie in the region of $\pm 0.5 \mu\text{m}$. Therefore, the TSVA network realizes virtual autofocusing with high accuracy.

3) *Influence of different test sets:* In this part, we examine the robustness of our method to different test sets. In Table III, we provide objective performance evaluation with respect to PSNR on samples of Dataset 2. It can be found that, for test samples from different resources of the training set, our method still achieves the best PSNR performance for all cases. The average PSNR gain over U-net is 3.49dB. The subjective performance comparison of U-net and TSVA is shown in Fig. 9 on Dataset 2. Similar to the results on Dataset 1, the structure errors produced by TSVA is also much smaller than U-net. These results demonstrate that the proposed TSVA network has a strong generalization capability.

VI. CONCLUSION

In this paper, we presented a high-speed and high-throughput whole slide imaging system. Traditional autofocusing methods rely on repetitive mechanical adjustment to conduct refocusing, which is time-consuming. Instead, our scheme does not perform autofocusing during the process of tissue slide scanning, but

TABLE IV

THE WORKFLOW COMPARISON BETWEEN THE CONVENTIONAL METHODS AND THE PROPOSED METHOD.

Step	Conventional Methods	Proposed Method
(a)	Create a z-stack for the first tile	Create a z-stack for the first tile
(b)	Predict the initial focal plane	Predict the initial focal plane
(c)	Repeat z-stack creating for other tiles	Repeat two-shot for other tiles
(d)	Create a focus map	Algorithm processing offline
(e)	Shift platform for in-focus shooting	Generate in-focus image directly

recovers the in-focus image based on two-shot ones in an offline learning-based manner, as shown in Table IV. The proposed method is built upon the well-known U-Net, which is modified and extended such that it can work with two input images and yields a recovered in-focus image. Experimental results demonstrate that our scheme achieves satisfactory performance on in-focus image recovery.

ACKNOWLEDGMENT

The authors would like to thank Prof. G. Zheng and Dr. S. Jiang from UCOON for sharing the real measurements for WSI setup and beneficial discussions about [14] as well as the following research.

REFERENCES

- [1] L. Pantanowitz, P. N. Valenstein, A. J. Evans, K. J. Kaplan, J. D. Pfeifer, D. C. Wilbur, L. C. Collins, and T. J. Colgan, "Review of the current state of whole slide imaging in pathology," *Journal of pathology informatics*, vol. 2, 2011.
- [2] R. S. Weinstein, A. R. Graham, L. C. Richter, G. P. Barker, E. A. Krupinski, A. M. Lopez, K. A. Erps, A. K. Bhattacharyya, Y. Yagi, and J. R. Gilbertson, "Overview of telepathology, virtual microscopy, and whole slide imaging: prospects for the future," *Human pathology*, vol. 40, no. 8, pp. 1057–1069, 2009.
- [3] C. Higgins, "Applications and challenges of digital pathology and whole slide imaging," *Biotechnic & Histochemistry*, vol. 90, no. 5, pp. 341–347, 2015.
- [4] E. Abels, L. Pantanowitz, F. Aeffner, M. D. Zarella, J. vd Laak, M. M. Bui, V. N. Vemuri, A. V. Parwani, J. Gibbs, E. Agosto-Arroyo *et al.*, "Computational pathology definitions, best practices, and recommendations for regulatory guidance: a white paper from the digital pathology association," *The Journal of pathology*, 2019.
- [5] E. Abels and L. Pantanowitz, "Current state of the regulatory trajectory for whole slide imaging devices in the usa," *Journal of pathology informatics*, vol. 8, 2017.
- [6] M. D. Zarella, D. Bowman, F. Aeffner, N. Farahani, A. Xthona, S. F. Absar, A. Parwani, M. Bui, and D. J. Hartman, "A practical guide to whole slide imaging: a white paper from the digital pathology association," *Archives of pathology & laboratory medicine*, vol. 143, no. 2, pp. 222–234, 2018.
- [7] P. Langehanenberg, G. von Bally, and B. Kemper, "Autofocusing in digital holographic microscopy," *3D Research*, vol. 2, no. 1, p. 4, 2011.
- [8] T. Kohlberger, Y. Liu, M. Moran, T. Brown, C. H. Mermel, J. D. Hipp, M. C. Stumpe *et al.*, "Whole-slide image focus quality: Automatic assessment and impact on ai cancer detection," *arXiv preprint arXiv:1901.04619*, 2019.
- [9] J. Liao, Y. Jiang, Z. Bian, B. Mahrou, A. Nambiar, A. W. Magsam, K. Guo, S. Wang, Y. ku Cho, and G. Zheng, "Rapid focus map surveying for whole slide imaging with continuous sample motion," *Optics letters*, vol. 42, no. 17, pp. 3379–3382, 2017.
- [10] M. C. Montalto, R. R. McKay, and R. J. Filkins, "Autofocus methods of whole slide imaging systems and the introduction of a second-generation independent dual sensor scanning method," *Journal of pathology informatics*, vol. 2, 2011.
- [11] J. Liao, L. Bian, Z. Bian, Z. Zhang, C. Patel, K. Hoshino, Y. C. Eldar, and G. Zheng, "Single-frame rapid autofocusing for brightfield and fluorescence whole slide imaging," *Biomedical optics express*, vol. 7, no. 11, pp. 4763–4768, 2016.
- [12] Y. Wu, Y. Rivenson, H. Wang, Y. Luo, E. Ben-David, L. A. Bentolila, C. Pritz, and A. Ozcan, "Three-dimensional virtual refocusing of fluorescence microscopy images using deep learning," *Nature methods*, vol. 16, no. 12, pp. 1323–1331, 2019.
- [13] H. Pinkard, Z. Phillips, A. Babakhani, D. A. Fletcher, and L. Waller, "Deep learning for single-shot autofocus microscopy," *Optica*, vol. 6, no. 6, pp. 794–797, 2019.
- [14] S. Jiang, J. Liao, Z. Bian, K. Guo, Y. Zhang, and G. Zheng, "Transform- and multi-domain deep learning for single-frame rapid autofocusing in whole slide imaging," *Biomedical optics express*, vol. 9, no. 4, pp. 1601–1612, 2018.

- [15] M. Subbarao and J.-K. Tyan, "Selecting the optimal focus measure for autofocusing and depth-from-focus," *IEEE transactions on pattern analysis and machine intelligence*, vol. 20, no. 8, pp. 864–870, 1998.
- [16] Y. Liron, Y. Paran, N. Zatorsky, B. Geiger, and Z. Kam, "Laser autofocusing system for high-resolution cell biological imaging," *Journal of microscopy*, vol. 221, no. 2, pp. 145–151, 2006.
- [17] M. Born and E. Wolf, *Principles of optics: electromagnetic theory of propagation, interference and diffraction of light*. Elsevier, 2013.
- [18] M. S. Hosseini, Y. Zhang, L. Chan, K. N. Plataniotis, J. A. Brawley-Hayes, and S. Damaskinos, "Focus quality assessment of high-throughput whole slide imaging in digital pathology," *arXiv preprint arXiv:1811.06038*, 2018.
- [19] J. G. McNally, T. Karpova, J. Cooper, and J. A. Conchello, "Three-dimensional imaging by deconvolution microscopy," *Methods*, vol. 19, no. 3, pp. 373–385, 1999.
- [20] D. A. Agard, "Optical sectioning microscopy: cellular architecture in three dimensions," *Annual review of biophysics and bioengineering*, vol. 13, no. 1, pp. 191–219, 1984.
- [21] C. Scofield, "212-d depth-of-field simulation for computer animation," in *Graphics Gems III (IBM Version)*. Elsevier, 1992, pp. 36–38.
- [22] O. Ronneberger, P. Fischer, and T. Brox, "U-net: Convolutional networks for biomedical image segmentation," in *Medical Image Computing and Computer-Assisted Intervention – MICCAI 2015*, N. Navab, J. Hornegger, W. M. Wells, and A. F. Frangi, Eds. Cham: Springer International Publishing, 2015, pp. 234–241.
- [23] J. Pan, D. Sun, H. Pfister, and M.-H. Yang, "Blind image deblurring using dark channel prior," in *Proceedings of the IEEE Conference on Computer Vision and Pattern Recognition*, 2016, pp. 1628–1636.
- [24] Y. Bai, G. Cheung, X. Liu, and W. Gao, "Graph-based blind image deblurring from a single photograph," *IEEE Transactions on Image Processing*, vol. 28, no. 3, pp. 1404–1418, 2018.
- [25] M. Aittala and F. Durand, "Burst image deblurring using permutation invariant convolutional neural networks," in *Computer Vision – ECCV 2018*, V. Ferrari, M. Hebert, C. Sminchisescu, and Y. Weiss, Eds. Cham: Springer International Publishing, 2018, pp. 748–764.
- [26] Y. Sun, S. Duthaler, and B. J. Nelson, "Autofocusing algorithm selection in computer microscopy," in *Intelligent Robots and Systems, 2005.(IROS 2005). 2005 IEEE/RSJ International Conference on*. Citeseer, 2005, pp. 70–76.
- [27] M. Hart, R. H. Barkhouser, M. Carr, M. Golebiowski, J. E. Gunn, S. C. Hope, and S. A. Smee, "Focal plane alignment and detector characterization for the subaru prime focus spectrograph," in *High Energy, Optical, and Infrared Detectors for Astronomy VI*, vol. 9154. International Society for Optics and Photonics, 2014, p. 91540V.
- [28] C. A. Schneider, W. S. Rasband, and K. W. Eliceiri, "Nih image to imagej: 25 years of image analysis," *Nature methods*, vol. 9, no. 7, p. 671, 2012.